DOI 10.1007/s11223-019-00075-8
Strength of Materials, Vol. 51, No. 2, March, 2019

DUCTILE-TO-BRITTLE TRANSITION AND IMPACT FRACTURE BEHAVIOR OF 3Mn–Si–Ni LOW CARBON MARTENSITIC STEEL

Y. J. Zhao,[a,b,1] Y. M. Su,[a] M. Liu,[a] Z. L. Hu,[b] and P. Tang[a,b,2]

UDC 539.4

Impact behavior related to crack initiation and growth of low carbon martensitic 3Mn–Si–Ni steel was investigated by instrumented impact Charpy V-notch tests. Load–displacement curves were acquired, so significant characteristic load parameters and impact absorbed energies in different fracture phases from 20~(−70)°C were determined. The ductile–brittle transition temperature (DBTT) was also investigated and the corresponding fractograph was obtained. The DBTT of the 3Mn–Si–Ni steel is −50°C. With the temperature decreased from 20 to −70°C, the maximum force F_m increases and the difference between the F_m and the crack stable propagation initial force F_{iu} decreases. Higher force was used to trigger the crack and tended to be brittle fracture at lower temperature, such as −50 and −70°C. Also once the crack initiated, it will extend rapidly until fracture when the tested steel serves at very low temperature, especially below −20°C. With the impact temperature decreasing to −70°C, the crack unstable growth final force F_a decreased to nearly zero and there isn't distinct secondary fiber area.

Keywords: ductile–brittle transition temperature, impact fracture behavior, instrumented Charpy impact, martensitic steel.

Introduction. In metals with a body-centered cubic (bcc) crystal structure, the fracture behavior usually changes from ductile to brittle with the temperature reduction. The ductile-to-brittle transition (DBT) temperature is a dominant index of measuring the brittle transition tendency of bcc metals, which determines the cryogenic toughness of the materials [1–3]. Therefore, DBT is a vital factor influencing the metal selection for components operating in low-temperature environment. For instance, railroad materials, ships that sail in cold waters and offshore platforms that are located in Arctic seas or deep oceans are extremely susceptible to DBT [4–7]. Charpy V-notch (CVN) impact test has been widely adopted to determine the DBT of various construction steels by the relationship between the absorbed energies and the impact temperatures [1, 2, 4, 8, 9], as shown in Fig. 1. In Fig. 1, there are three typical regions, namely the brittle region (low temperature region), the transition region, and the ductile region (high temperature region). In the low temperature region, the fracture mode is brittle, such as cleavage, whereas in the high temperature region, the fracture mode is ductile. Ductile fracture is usually initiated by the joining of the growing microvoids, which neighbor the heavily deformed crack tip [4, 10]. Brittle cleavage fracture is usually initiated by the propagation of unstable cracks along cleavage planes and the above unstable cracks usually originate from cracked second-phase particles or non-metallic particles [4, 11]. On the other hand, fracture behavior in the transition region is quite complicated because both cleavage and ductile tearing failures compete with each other [12, 13]. Ductile–brittle transition temperature (DBTT) can be referred to as the transition of fracture mode, and it is often

[a]School of Resources, Environment and Materials, Guangxi University, Nanning, Guangxi, China [[1]zhaoyanjun71@163.com (Yan-jun Zhao); [2]tp@gxu.edu.cn (Peng Tang)]. [b]Guangxi Key Laboratory of Processing for Non-Ferrous Metal and Featured Materials, Nanning, Guangxi, China. Translated from Problemy Prochnosti, No. 2, pp. 142 – 152, March – April, 2019. Original article submitted August 3, 2018.

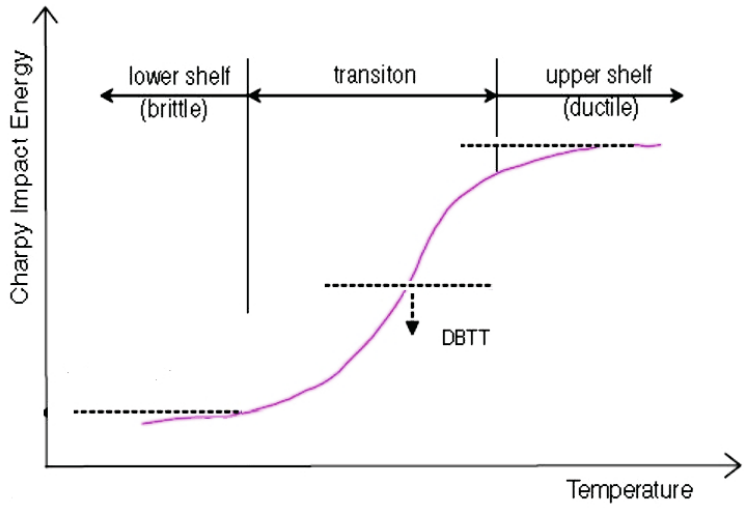

Fig. 1. The relationship between Charpy V-notch impact energy and temperature and DBTT.

determined by the temperature corresponding to the average of the upper- and low-shelf energies in the CVN impact energy curve.

According to ASTM A370 [14], CVN impact test frequently uses simple full-sized ($10 \times 10 \times 55$ mm) rectangular specimens with a V- or U-type notch of specified geometry (2 mm-deep). During the notched specimen fracture by a single blow in a simple pendulum impact tester, the total dynamic energy absorption of crack initiation, extension and fracture can be assessed. However, partial energies absorbed at different phases of fracture process, such as ductile crack front initiation and extension, cleavage fracture, and crack arrest, cannot be provided by such tests. Instrumented Charpy impact test equipment can continuously record data on displacement, force, energy, time, etc., and save them in PC [15–18]. Therefore, further valuable information on the material fracture behavior under impact loading conditions could be provided by modified instrumented Charpy testing technique, especially after strain gauges were introduced in 1930 [19, 20] and several fracture mechanics parameters of numerous metals and alloys were developed [16–18]. Additionally, Kobayashi et al. developed a new dynamic fracture toughness testing system, in which some fracture mechanics parameters such as *J*-integral, stress intensity factor (K_I) and absorbed energies could be achieved [21, 22]. Finally, the instrumented Charpy impact test can provide useful comparative quantitative data with relatively simple testing procedures and easily manufactured specimens.

The DBTT is closely related to the change of fracture mode and material capability of energy absorption during its fracture. However, the availability of instrumented impact data on bcc metals is still limited, and there is no clear relationship between the CVN impact energy and fracture toughness yet. In this research, a low carbon 3Mn–Si–Ni martensitic structural steel was investigated, and its crack initiation and growth pattern were analyzed using instrumented Charpy impact tests. The relationships among the crack initiation and growth behavior, fracture morphology, and absorbed impact energy were investigated, in order to provide the basis for analysis of impact fracture mechanism of ductile iron. Furthermore, the tested steel tensile strength and V-notch impact toughness are more than 1500 MPa and 85 J, respectively [24]. It can be used as the tamping tine for the railway maintenance sustaining severe conditions such as high speed, continuous cycle reciprocating collision. However, the long-term exposure to cold air in cold regions brings brittleness to the components. Therefore, the steel DBTT in the range from –70 to 20℃, and its dependence on the steel chemical composition are discussed to ensure the steel high reliability.

1. Experimental Procedure and Methodology.

1.1. Material. The tested material, namely 3Mn–Si–Ni steel, is a high-strength and high-toughness martensitic steel, which chemical composition and mechanical properties are listed in Tables 1 and 2 [23], respectively. The ingots were prepared using a vacuum induction furnace with a capacity of 130 kg, followed by hot forging to 50 mm thickness, slow-cooled to 680℃, and annealed at this temperature for achieving good machinability.

TABLE 1. Chemical Composition of 3Mn–Si–Ni, AISI-1018, and DP590 Steels (wt.%)

Steel	C	Si	Mn	Ni	Ti	Cr	P	S	Fe
3Mn–Si–Ni	0.19	1.19	2.83	1.24	0.049	0.031	< 0.016	< 0.0045	Bal.
AISI-1018	0.14–0.20		0.60–0.90				< 0.040	< 0.05	Bal.
DP590	0.08		1.24				0.018	0.005	Bal.

TABLE 2. Mechanical Properties of the 3Mn–Si–Ni, AISI-1018, and DP590 Steels

Steel	Yield strength (MPa)	Ultimated tensile strength (MPa)	Elongation (%)
3Mn–Si–Ni	1250	1550	16
DP590	350	602	24–30
AISI-1018	275	475	38

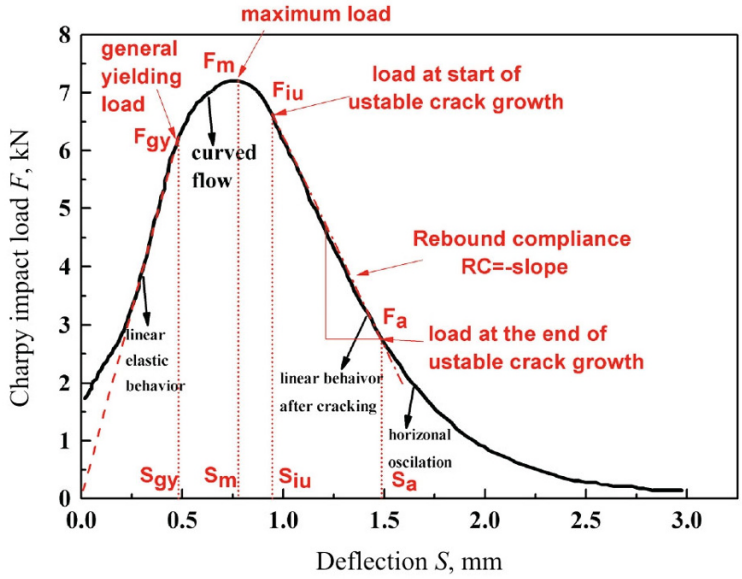

Fig. 2. Graphical illustration of characteristic impact loads for a Charpy impact load–deflection curve.

Following these procedures, the steel was austenitized at 900℃ for 40 min, oil-quenched and air-cooled to 230℃, held at the temperature for 120 min, and then air-cooled to room temperature. AISI-1018 and DP590 steels were used as reference materials to be compared with 3Mn–Si–Ni steel, and their chemical composition and mechanical properties [24, 25] are listed in Tables 1 and 2, respectively.

1.2. Procedure and Methodology. The specimens with $10 \times 10 \times 55$ mm dimensions, in accordance with the ASTM Standard E23, were prepared along the longitudinal direction (which is indicated as *L* in the following test abbreviations). A Ni500 pendulum impact tester, equipped with an instrumented striker, was used. Strain gauges were attached to both sides of the striker tup to record the specimens deflection and the impact force applied to the specimen. After suitable conversion, a load–displacement curve could be plotted, providing such essential characteristic load parameters as the maximum fracture load (F_m), general yield load (F_{gy}), crack arrest load (F_a), and unstable crack initiation load (F_{iu}).

Figure 2 illustrates a typical impact load–deflection curve, which was presented by Alexopoulous et al. [24]. The curve can be subdivided into four parts: linear elastic behavior, serratic flow, linear behavior after cracking, and horizontal oscillation. The general yield load F_{gy} represents the end of elastic deformation and the start of plastic deformation, which is evaluated from the transition of the linear elastic behavior to the serratic flow, F_m is the

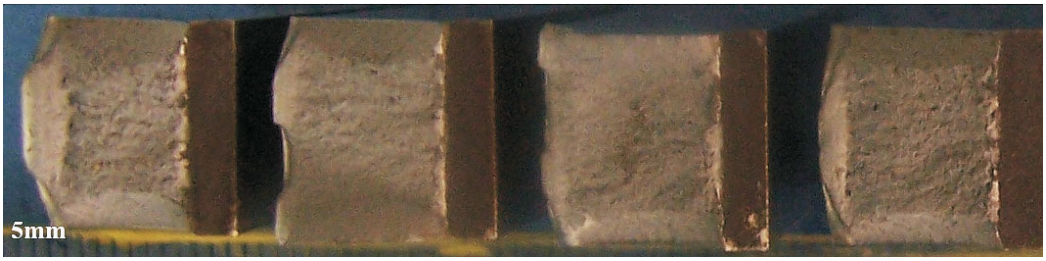

a b c d

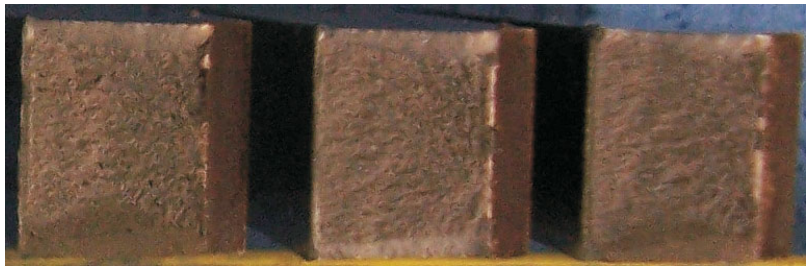

e f g

Fig. 3. Macrografs of the impact fracture surfaces of 3Mn–Si–Ni steel at different temperatures: (a) 20℃; (b) 0℃; (c) –20℃; (d) –50℃; (e) –60℃; (f) –70℃; (g) –80℃.

maximum impact load, F_{iu} relates to the start of unstable crack growth, which is evaluated as the linear behavior onset, and F_a corresponds to the end of unstable crack growth, which is determined as the end of the linear behavior. Rebound compliance is determined by the slope of impact load–deflection from F_{iu} to F_a. Corresponding deflections (S_{gy}, S_m, S_{iu}, and S_a) are also indicated.

Characteristic load points can be determined by means of impact load–deflection curve (Fig. 2). The energy consumed for a given deflection can be calculated as the integral of the impact load–deflection curve. $W_{cracking}$ can be calculated as follows:

$$W_{cracking} = W_m + W_{iu} + W_a = \int_0^{F_m} F(S)dS + \int_{F_m}^{F_{iu}} F(S)dS + \int_{F_{iu}}^{F_a} F(S)dS, \quad (1)$$

where $W_{cracking}$ is the absorbed impact energy, W_m is nucleation energy of the crack ahead the V-notch, and W_{iu} and W_a are stable and unstable crack growth energies, respectively.

1.3. Test Temperature and Microstructural Observations. The test temperature ranged from 20 to –70℃. When the temperature was below room temperature, the specimen was cooled using liquid nitrogen; when the temperature was above room temperature, the specimen was heated using hot water. The fractography was characterized using a CAMBRIDGE scanning electron microscopy (SEM) operated at 20 kV.

2. Results and Discussion.

2.1. Relation between Fractography and Characteristic Impact Loads. Figure 3 shows the macrographs of fracture surfaces of specimens at the test temperatures of 20, 0, –20, –50, –60, –70, and –80°C. Specimens at 20 and 0℃ exhibited a macroscopic ductile behavior with lateral expansions of 0.68 and 0.57 mm, respectively. In contrast, specimens at (–60) ~ (–80)℃ were mainly brittle, with narrow regions of shear lips at their edges.

Figure 4 shows the relation between macrofractography and characteristic impact force. The initial crack began at the root of the specimen notch, and then plastic deformation and hardening occurred, which increased the impact force. Before the impact force reached the maximum F_m, the crack became extended, and both faces of the specimen notch begin to contact each other. After that, the crack grew further until the force F_{iu} was reached, which corresponded to the crack stable propagation forming a heel-shaped fiber area. When the impact force decreased

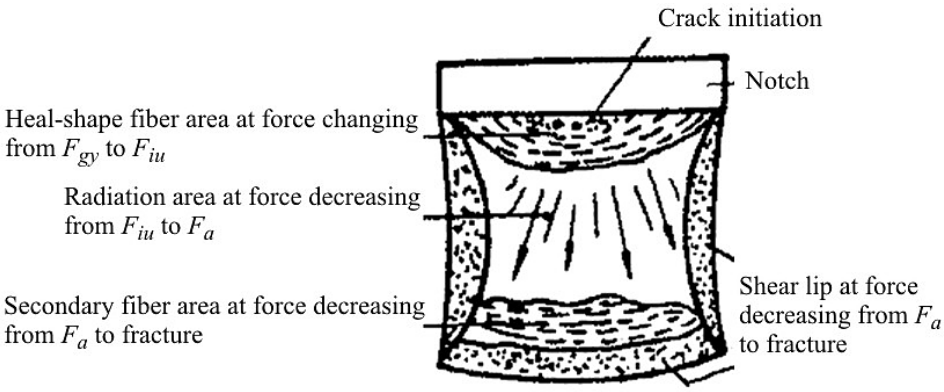

Fig. 4. Relation between macrofractography and impact force.

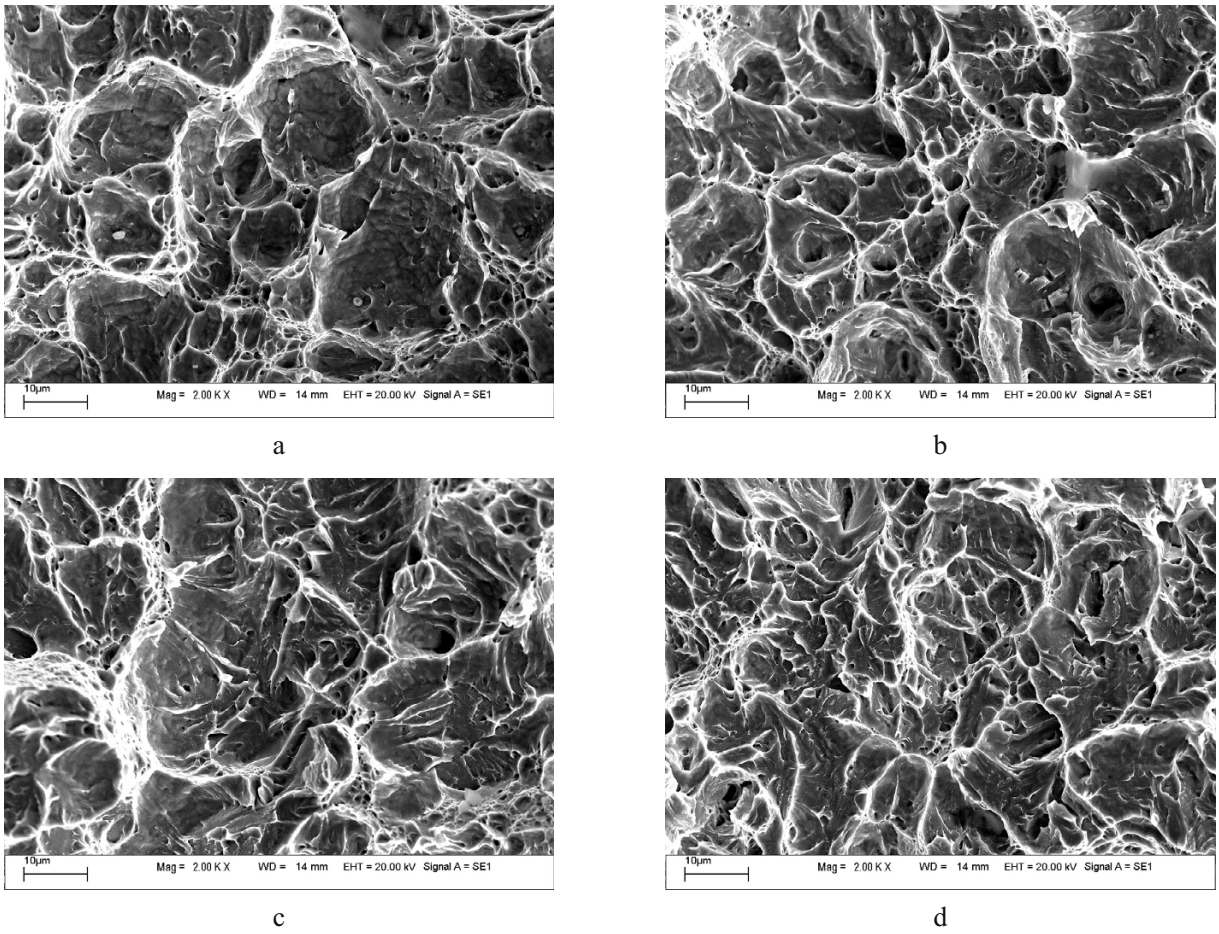

Fig. 5. SEM images of the impact fracture surface of 3Mn–Si–Ni steel (center) at different temperatures: (a) 20℃; (b) 0℃; (c) −50℃; (d) −70℃.

from F_{iu} to F_a, the unstable crack propagation was observed. So, the radiation area size depends on the difference value between F_{iu} and F_a, which represents the test steel brittleness. The higher is this difference value, the larger is radiation area. After reaching F_a, the force decreased slowly, and the shear lip and secondary fiber area were formed. At high values of F_a, the secondary fiber area may appear, at lower ones it may disappear.

Figure 5 shows the SEM microscopic features in the center zone of specimens tested at 20, 0, −50, and −70℃, respectively. At 20℃, many deep equiaxed dimples of ~ 20 μm of diameter were observed, indicating a

TABLE 3. Characteristic Values at Different Temperatures

Temperature (℃)	Yield force F_{gy}, kN	Peak force F_m, kN	Crack propagation initial force F_{iu}, kN	Crack propagation final force F_a, kN	Crack propagation initial displacement S_{iu}, mm	Crack propagation final displacement S_a, mm
20	14.5	22.7	21.7	13.3	2.2	2.3
0	17.5	24.0	23.2	11.0	2.2	2.3
–20	18.0	28.0	28.0	9.7	1.9	2.2
–50	19.2	29.3	28.9	9.6	1.9	2.0
–70	19.9	31.7	30.9	2.4	1.9	1.9

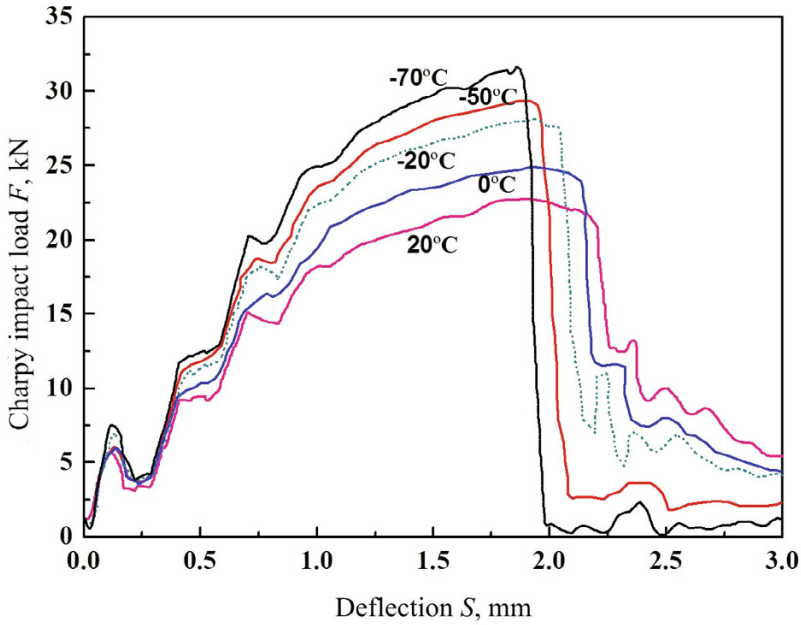

Fig. 6. The impact force–deflection curves at different temperatures of 3Mn–Si–Ni steel.

ductile fracture. At 0℃, shallower and coarser dimples were observed, as compared to those at 20℃. At −50℃, although few shallow and small dimples still existed, the cleavage pattern of the order of marble and quasi-cleavage facets were predominant, which implied brittle fracture. At −70℃, only cleavage patterns were observed.

2.2. Effect of Temperature on Characteristic Values and Impact Energy. Charpy impact load–deflection curves at different temperatures are shown in Fig. 6. Corresponding characteristic values are listed in Table 3. Figure 6 shows that the maximum force F_m was equal to 22.7 kN at 20℃, 28 kN at −20℃, and 31.7 kN at −70℃. Therefore, with the temperature decrease, the maximum force F_m increased and the rate of the strain hardening increased. That means that a higher force was required to trigger the crack propagation, and the fracture tended to be brittle at lower temperature. When the 3Mn–Si–Ni steel was tested in the temeprature range [(−20) ~ (−70)℃], the fracture was more readily produced by the impact load. With the impact temperature drop, the difference between F_{iu} and F_a increased, while that between S_{iu} and S_a decreased. Therefore, the crack unstable propagation rate, which is also refferred to as rebound compliance, increased.

The evolution of impact energy with deflection is shown in Fig. 7. The impact energy for different stages is summarized in Table 4. With a temperature drop, the crack initiation energy increased. The energy values corresponding to S_m, S_{iu}, and S_a at 20 and −20℃ increased with the deflection, however the energy value did not change after the deflection reached S_a at −70℃. Therefore, the total energy consumed to form the shear lip and secondary fiber area was nearly zero, while the main energy was used to initiate the crack at −70℃. With the impact temperature drop to −70℃, there was no distinct secondary fiber area observed, and F_a value decreased to nearly

TABLE 4. Impact Energy Related to Characteristic Values at Different Temperatures

Temperature (℃)	Energy at peak load W_m, J	Crack propagation initial energy W_{iu}, J	Crack propagation final energy W_a, J
20	27.9	43.9	45.8
0	36.7	42.9	46.9
–20	35.9	35.7	41.0
–50	33.1	33.3	35.3
–70	37.2	37.9	39.6

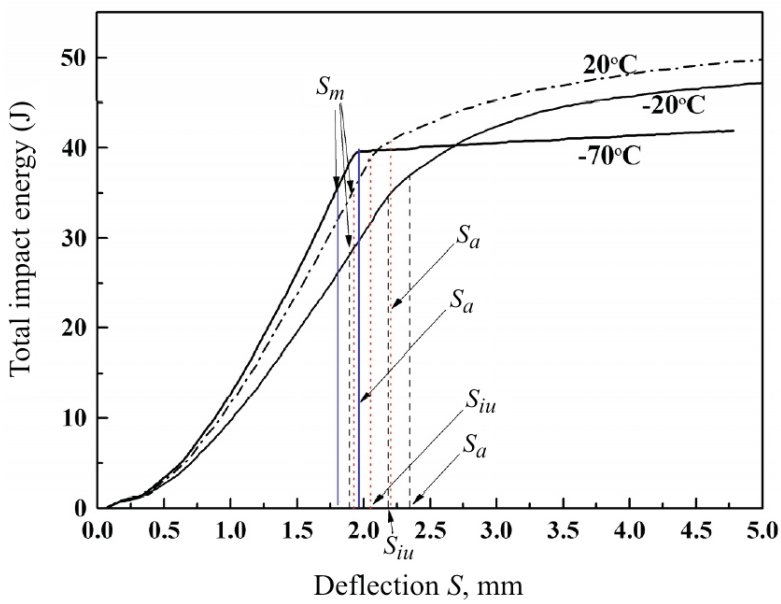

Fig. 7. Absorbed impact energy–deflection curves of 3Mn–Si–Ni steel at 20, –20, and −70℃.

zero. With the impact temperature rise, the difference between S_m and S_{iu} increased, and the energy between S_m and S_{iu} was mainly used to form deeper and larger dimples. This implies that more energy is required to provide the crack propagation and increase the material toughness before fracture. As a result, the steel toughness is improved with the test temperature rise.

The energy required for a stable crack propagation is the largest at 20℃. With an increase in temperature, this energy value drops, resulting in a faster crack growth. In particular, this energy nearly dropped to zero at −70℃, indicating a ductile brittle fracture at low temperatures.

2.3. DBTT Dependence on Chemical Composition. DBTT is determined by the temperature corresponding to the average of the upper- and low-shelf energies. In Fig. 8, the low-shelf energy is 33 J and the upper-shelf one is 70~73 J for the 3Mn–Si–Ni steel, so the average temperature was about −50℃. As a result, the DBTT should be about −50℃, according to energy- and fractography-based estimations (Figs. 3 and 5).

Figure 8 also shows the CVN energy of AISI-1018 and DP590 steels. The trend of temperature–CVN impact energy curve is closely related to the material chemical composition. Although Mn content in AISI-1018 steel is much lower than those in DP590 and 3Mn–Si–Ni steels, its impact energy is the lowest, mainly due to high S and P contents. The fracture triggering sites of Charpy specimens have been identified: large facets with low misorientations (type I), iron carbides or second phase particles (such as TiC) (type II), manganese sulfide inclusions (type III), ductile tearing zone (type IV) or nonidentified sites (type V) [9, 25]. Although AISI-1018 and 3Mn–Si–Ni steels have nearly the same C content, a lower S content in the latter steel leads to a lower propensity to form MnS

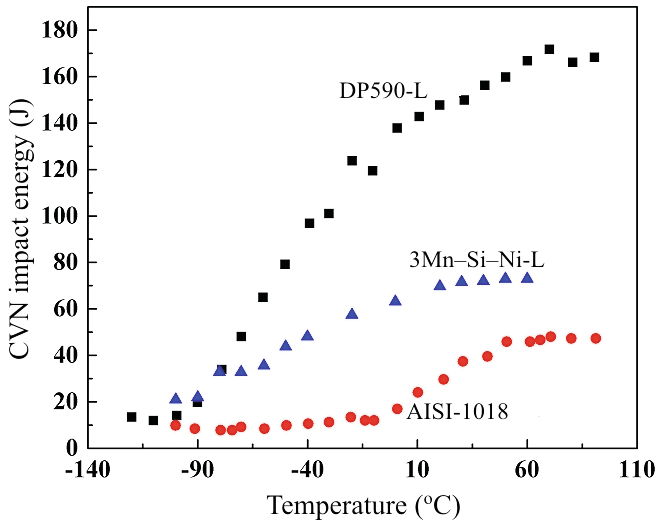

Fig. 8. Effect of chemical compositons on the CVN impact energy.

inclusions, which greatly hinder its fracture triggering sites (such as types II and III). Therefore, the DBTT of 3Mn–Si–Ni steel is lower than that of AISI-1018 steel. For DP590 and 3Mn–Si–Ni, their S and P contents are almost equal, but the latter's C and Mn contents are much higher than those of the former steel, which greatly enhances the fracture triggering sites (such as types II and III). Thus, the DBTT of 3Mn–Si–Ni steel is higher than that of AISI-1018 steel.

Conclusions. The Charpy V-notch impact energy of 3Mn–Si–Ni steel is experimentally investigated using the instrumented Charpy V-notch impact test at test temperatures ranging from 20 to −70℃.

1. Load–displacement curves of 3Mn–Si–Ni steel were constructed, from which important characteristic load parameters and absorbed energies at various phases of fracture from 20 to −70℃ were determined.

2. When the test temperature dropped from 20 to −70℃, the maximum force F_m increased, whereas the difference between F_m and F_{iu} values decreased. This implies that higher force is required to trigger the crack propagation and, thus, brittle fracture occurs at lower temperatures. At temperatures below −20℃, once the crack is initiated, it will extend rapidly until the final fracture. When the impact test temperature dropped to −70℃, the value F_a decreased to nearly zero, and no distinct secondary fiber area was observed.

3. The DBTT of 3Mn–Si–Ni steel was assessed as −50℃ based on the combined analysis of the energy process and fractographs. The effect of Mn content on the DBTT strongly depends on the contents of C and S.

Acknowledgments. This work was financially supported by the National Natural Science Foundation of China (No. 51661004), Guangxi Key Laboratory of Processing for Non-Ferrous Metal and Featured Materials of China (No. GXYSSF1809), and Guangxi Natural Science Foundation of China (No. 2017GXNSFAA198271).

REFERENCES

1. T. Tagawa, Y. Kayamori, and H. Hira, "Statistical scatter of fracture toughness in the ductile–brittle transition of a structural steel," *Eng. Fract. Mech*., **77**, No. 16, 3077–3086 (2010).
2. S. L. Chen, J. Hu, X. D. Zhang, et al., "High ductility and toughness of a micro-duplex medium-Mn steel in a large temperature range from −196℃ to 200℃," *J. Iron Steel Res. Int.*, **22**, No. 12, 1126–1130 (2015).
3. A. Pineau, "Modeling ductile to brittle fracture transition in steels – micromechanical and physical challenges," *Int. J. Fracture*, **150**, Nos. 1–2, 129–156 (2008).
4. A. Gopalan, M. K. Samal, and J. K. Chakravartty, "Fracture toughness evaluation of 20MnMoNi55 pressure vessel steel in the ductile to brittle transition regime: Experiment & numerical simulations," *J. Nucl. Mater.*, **465**, 424–432 (2015).

5. J. R. Shaw and B. K. Zuidema, *New High Strength Steels Help Automakers Reach Future Goals for Safety, Affordability, Fuel Efficiency and Environmental Responsibility*, SAE Technical Paper 2001-01-3041 (2001), doi: 10.4271/2001-01-3041.
6. G. Krauss, *Steels: Processing, Structure, and Performance*, ASM International, Materials Park, OH (2005).
7. Y. N. Liu, Y. R. Feng, Q. R Ma, and X. L. Song, "Dynamic fracture toughness of X70 pipeline steel and its relationship with arrest toughness and CVN," *Mater. Design*, **23**, No. 8, 693–699 (2002).
8. Y. J. Chao, J. D. Ward, and R. G. Sands, "Charpy impact energy, fracture toughness and ductile–brittle transition temperature of dual-phase 590 steel," *Mater. Design*, **28**, No. 2, 551–557 (2007).
9. B. Tanguy, J. Besson, R. Piques, and A. Pineau, "Ductile to brittle transition of an A508 steel characterized by Charpy impact test: Part I: Experimental results," *Eng. Fract. Mech.*, **72**, No. 1, 49–72 (2005).
10. P. Haušild, I. Nebdal, C. Berdin, and C. Prioul, "The influence of ductile tearing on fracture energy in the ductile-to-brittle transition temperature range," *Mater. Sci. Eng. A*, **335**, Nos. 1–2, 164–172 (2002).
11. A. R. Rosenfield, D. K. Shetty, and A. J. Skidmore, "Fractographic observations of cleavage initiation in the ductile-brittle transition region of a reactor-pressure-vessel steel," *Metall. Trans. A*, **14**, No. 9, 1934–1937 (1983).
12. X. N. Zhang, Y. D. Qu, and R. D. Li, "Low temperature impact toughness and fracture analysis of EN-GJS-400-18-LT ductile iron under instrumented impact load," *J. Iron Steel Res. Int.*, **22**, No. 9, 864–869 (2015).
13. M. K. Samal, J. K. Chakravartty, M. Seidenfuss, and E. Roos, "Evaluation of fracture toughness and its scatter in the DBTT region of different types of pressure vessel steels," *Eng. Fail. Anal.*, **18**, No. 1, 172–185 (2011).
14. *ASTM E23-96. Standard Test Method for Notched Bar Impact Testing of Metallic Materials*, Annual Book of ASTM Standards, Philadelphia, PA (1996).
15. A. Rossoll, C. Berdin, and C. Prioul, "Determination of the fracture toughness of a low alloy steel by the instrumented Charpy impact test," *Int. J. Fracture*, **115**, No. 3, 205–226 (2002).
16. S. S. M. Tavares, M. B. Silva, M. C. S. de Macêdo, et al., "Characterization of fracture behavior of a Ti alloyed supermartensitic 12%Cr stainless steel using Charpy instrumented impact tests," *Eng. Fail. Anal.*, **82**, 695–702 (2017).
17. H. S. Shin and B. J. Tuazon, "An instrumented drop-bar impact testing apparatus for investigating the impact fracture behaviors of structural steels," *Int. J. Impact Eng.*, **84**, 124–133 (2015).
18. E. Lucon, "Estimating dynamic ultimate tensile strength from instrumented Charpy data," *Mater. Design*, **97**, 437–443 (2016).
19. M. Tanaka, and S. Umekawa, "On the breaking behaviour in Charpy impact bending tests," in: Proc. of the 1st Japan Congress for Testing Materials (1958), p. 95.
20. S. Ono, "Micro-time structure of impact fracture concerning Charpy test," in: Proc. of the 1st Japan Congress for Testing Materials (1958), p. 98.
21. T. Kobayashi, "On the information about fracture characteristics obtained from instrumented impact test of A533 steel for reactor pressure vessel," *Eng. Fract. Mech.*, **19**, No. 1, 67–79 (1984).
22. T. Kobayashi, and M. Niinomi, "Evaluation of dynamic crack initiation and growth toughness by computer aided Charpy impact testing system," *Nucl. Eng. Des.*, **111**, Nos. 1–2, 27–33 (1989).
23. Y. J. Zhao, L. W. Xu, L. P. Yan, et al., "Investigation on a new low alloy high strength and high toughness Mn steel," *J. Univ. Sci. Technol. B.*, **32**, No. 2, 196–201 (2010).
24. N. D. Alexopoulos, A. Stylianos, and J. Campbell, "Dynamic fracture toughness of Al–7Si–Mg (A357) aluminum alloy," *Mech. Mater.*, **58**, 55–68 (2013).
25. D. Rittel, B. Tanguy, A. Pineau, and T. Thomas, "Impact fracture of a ferritic steel in the lower shelf regime," *Int. J. Fracture*, **117**, No. 2, 101–112 (2002).